Measurement Science
and Technology

ACCEPTED MANUSCRIPT

Precision 3D Volume Measurement of Transparent Adhesives via Spectr ally Optimized Line Laser Scanning and Enhanced Centroid Extraction

To cite this article before publication: Ling Cao *et al* 2025 *Meas. Sci. Technol.* in press https://doi.org/10.1088/1361-6501/ae1a9f

IOP Publishing Journal Title
Journal **XX** (XXXX) XXXXXX https://doi.org/XXXX/XXXX

Precision 3D Volume Measurement of Transparent Adhesives via Spectrally Optimized Line Laser Scanning and Enhanced Centroid Extraction

Ling Cao[1], Renjie Zhou[2], Xinhua Wang[2], Wei Pan[*]

[1]Author is with College of Electronics and Information Engineering, Shenzhen University, Shenzhen, China (email: caoling@optmv.com)

[2]Authors are with Guangdong Polytechnic Normal University, Guangzhou, China (email: renjiezhou@stu.gpnu.edu.cn, wangxh@gpnu.edu.cn)

[*]Author is *Corresponding author with OPT Machine Vision, Dongguan, China (email: vpan@foxmail.com)

Abstract

Accurate 3D volume measurement of transparent adhesives is essential for ensuring dispensing quality and production efficiency in precision manufacturing. We present a robust line laser scanning system enhanced by automatic camera calibration and complementary spectral background optimization (CSBO), which improves 3D reconstruction accuracy by suppressing transmitted light and internal reflections—without complex ray-tracing models. A novel subpixel laser stripe centroid extraction algorithm is further introduced, integrating a candidate point mechanism with a dynamic weighted multi-factor scoring strategy (DWMF-SS) to enhance stability and noise robustness. Experiments show that the proposed centroid extraction method surpasses conventional approaches in precision and interference resistance, while the CSBO method achieves a minimum relative volume error of 1.62% against ground truth, enabling real-time industrial measurement of transparent materials.

Keywords: 3D reconstruction, volume measurement, laser scanning, transparent object measurement, 3d metrology

1. Introduction

Manual adhesive dispensing, commonly used in electronic packaging and precision manufacturing, often results in inconsistent quality and low efficiency, thereby impeding progress toward high-precision industrial production. Automated dispensing machines [1] overcome these challenges by employing precise control mechanisms to ensure accurate adhesive application via techniques such as dot dispensing, line drawing, and complex coatings. This technology is extensively employed in precision manufacturing processes across the electronics [2], automotive, and medical industries, providing crucial technical support to improve productivity and elevate product reliability.

Conventional pneumatic dispensers regulate adhesive deposition through air pressure magnitude and valve actuation duration. However, inherent system limitations, particularly fluctuations in air pressure, pose significant challenges to maintaining uniform adhesive discharge. Excessive material deposition may induce adhesive overflow, while insufficient discharge risks causing inadequate bonding strength or compromised airtightness. These issues ultimately lead to product performance failures and quality deterioration. Furthermore, inaccurate adhesive dispensing can also instigate rework operations and material waste, escalating production costs. Consequently, the precise

volume measurement of dispensed adhesive serves as a critical process control node, providing essential data-driven guidance for calibration of adhesive discharge, with direct implications for enhanced product quality and manufacturing efficiency.

Existing adhesive volume measurement techniques include manual methods, ultrasonic approaches [3], electrochemical systems [4], and optical non-contact 3D methods [5]. Manual methods typically utilize electronic calipers to track piston trajectories, combined with adhesive formulation ratio calculations. However, this approach exhibits inherent limitations, including time-consuming procedures, measurement inaccuracies, and elevated labor costs, failing to satisfy modern industrial demands for precision and operational efficiency. Ultrasonic methods estimate volume by analyzing propagation time, reflected signals, and attenuation but are sensitive to material properties and environmental variations, which compromises measurement accuracy. Electrochemical methods, limited by the dielectric nature of most adhesives, struggle to achieve reliable industrial applications. Advancements in optical imaging have positioned 3D vision inspection as a prominent focus of research and development. Optical non-contact 3D methods capture surface light reflection patterns to acquire geometric and optical data [6], reconstructing high-precision 3D models in real time. By integrating image processing with 3D data analysis, these systems excel in applications such as defect inspection, outperforming other methods in accuracy and stability, particularly for opaque materials.

Traditional reflection-based 3D measurement methods (e.g., structured light projection [7-9], photometric stereo [10-11], and stereo vision [12-13]) demonstrate significant limitations when applied to transparent object, and typically exhibit substantial measurement inaccuracies or even fail to achieve complete reconstruction. Phase shifting profilometry (PSP) performs well for objects with diffuse surfaces, as it relies on accurate intensity values from captured fringe patterns. However, for transparent objects such as glass, reflections from both front and back surfaces overlap, causing intensity aliasing in the recorded fringes [14].

This technical constraint primarily stems from the fundamental incompatibility between transparent surfaces and the diffuse reflection assumption inherent in these conventional methods, rendering them inherently unsuitable for direct application in the 3D reconstruction of transparent objects. The optical interaction between transparent objects and incident light is highly complex, including multiple reflection and refraction phenomena that pose substantial challenges for optical path tracing [15]. Furthermore, transparent materials inherently lack distinct surface textural features, instead exhibiting environmental distortion patterns that are susceptible to viewpoint variations and ambient interference. The refractive behavior of these materials is dependent on spatially varying and potentially non-uniform refractive indices, which further compounds the analytical complexity of optical path determination [16]. These factors significantly amplify the complexity of 3D data acquisition, feature matching, and data processing, presenting formidable challenges for 3D reconstruction and volume measurement of transparent adhesives. The intricate and irregular geometric shapes formed during adhesive dispensing further exacerbate measurement difficulties, imposing rigorous performance requirements on 3D imaging systems and noise-resistant algorithms.

In recent years, researchers have developed a variety of laser scanning fusion technologies to overcome these challenges. He et al. [17] developed an innovative laser tracking frame to frame strategy capable of effectively detecting and discriminating laser lines reflected from the anterior surfaces of transparent objects. This single-scanning approach with secondary reflection modelling enables 3D morphological reconstruction of anterior surfaces, providing a novel solution for 3D reconstruction of optically complex transparent materials. Despite its effectiveness, this approach leads to a significant increase in computational cost due to complex ray-tracing algorithms. Building upon prior advancements, He et al. [18] developed a multi-stage surface reconstruction framework for transparent materials, which employs a four-tier refinement architecture. This method progressively extracts primary reflection points from 3D candidate clusters, and demonstrates enhanced stability and precision compared to conventional laser scanning techniques. However, this approach remains susceptible to interference from severe cross-reflections, which manifests as reconstruction to ineffective candidate feature point discrimination, thereby compromising both reconstruction clarity and dimensional accuracy. In addition, this stereo imaging system elevates hardware implementation costs.

This study designed a volume measurement system for transparent adhesives, aiming to overcome the limitations of current methods in transparent adhesives discharge calibration. The proposed system utilizes a traditional monocular line laser scanning system [19-20] to acquire higher precision transparent adhesives depth map data. Furthermore, multi-stage 3D reconstruction and geometry analysis algorithms were employed to achieve high precision measurements of transparent adhesives volume. The primary contributions of this article are as follows.

1) We proposed an automatic camera calibration method. By simplifying the calibration process and eliminating secondary calibration steps, this method not only reduces cumulative errors but also enhances production efficiency
2) An improved laser stripe centroid extraction method was proposed, which is based on the gray-level center of gravity approach and incorporates a novel candidate point selection mechanism along with the DWMF-SS metho

d. DWMF-SS integrates multiple scoring criteria to achi eve robust sub-pixel localization, reducing errors from s ingle-variable approaches and improving stability and p recision.

3) We proposed a CSBO method by leveraging the comple mentary transmitted light absorption properties of the b ackground substrate, which effectively mitigates interna l laser scattering and reflection interference. Without co mplex ray-tracing algorithms and auxiliary equipment, t his optical method significantly enhances 3D reconstruc tion accuracy of transparent adhesives.

4) This volume measurement system integrated into adhesi ve dispensing workflows enables high precision volume measurement of transparent adhesives, providing precis e data-driven guidance and real-time feedback mechani sm for adhesive discharge calibration. This system can be used for measuring various types of such materials.

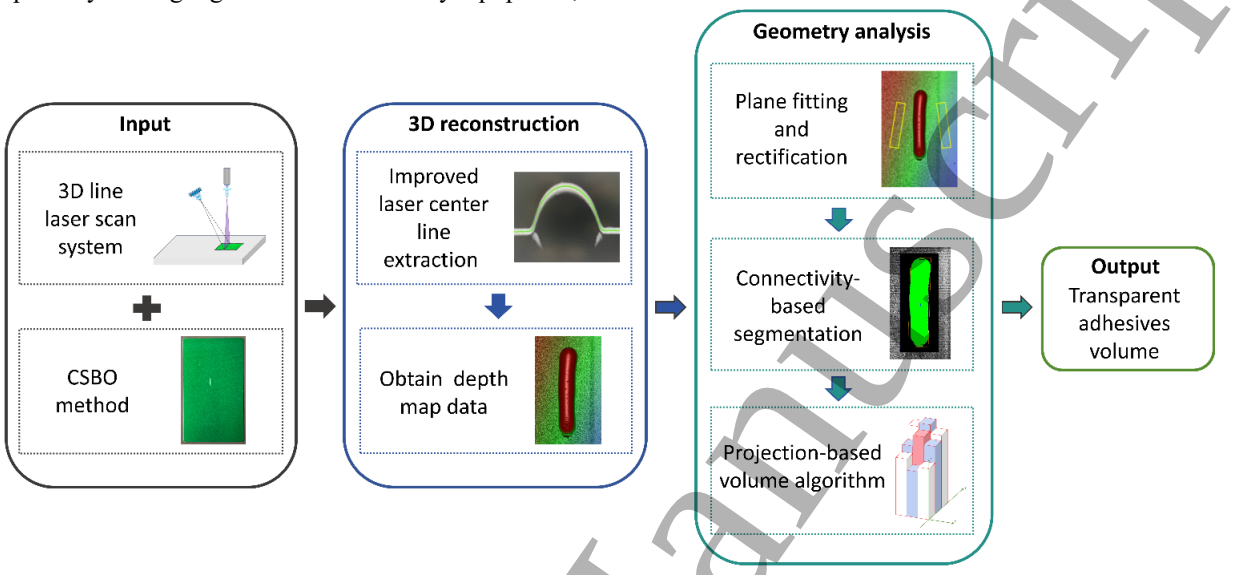

Figure 1. Flowchart of the system algorithm.

2. Imaging optimization method and 3D system calibration

The system algorithm flow is shown in Figure 1. We employs a line laser scanning system enhanced by automatic camera calibration and complementary spectral background optimization (CSBO). Furthermore, we propose a novel laser stripe centroid extraction algorithm for 3D reconstruction, followed by geometry analysis of the reconstructed data to obtain the volume of transparent adhesives.

2.1. Complementary spectral background optimization

As shown in Figure 2, the proposed CSBO method employs a dispensing nozzle to extrude transparent adhesives onto the green-yellow substrate with green-yellow spectral absorption characteristics [21], which serves as background panels for specimen preparation and experimental design. The underlying principle exploits wavelength-selective absorption, where materials exhibit wavelength-dependent optical interactions through preferential absorption of specific spectral bands while transmitting or reflecting others. This quantum mechanical phenomenon is governed by discrete energy states inherent to atomic systems, wherein electron transitions to elevated energy states occur through resonant photon absorption when incident photon energy corresponds to the inter-state energy differential [22]. The expression for photon energy $\boldsymbol{E}$ and the inter-state energy differential $\boldsymbol{\Delta E}$ is as follows:

$$E = h * f = \frac{h * c}{\lambda} \#(1)$$

$$\Delta E = E_{excited\ state} - E_{ground\ state} = \frac{h * c}{\lambda_{absorbed}} \#(2)$$

Where $\boldsymbol{\lambda}$ is wavelength of absorbed light, $\boldsymbol{f}$ denotes the optical frequency, $\boldsymbol{h}$ represents Planck's constant, and $\boldsymbol{c}$ corresponds to the speed of light, $\boldsymbol{\lambda_{absorbed}}$ is wavelength of absorbed light. Consequently, material-specific energy level differences induce wavelength-selective photon absorption, thereby generating distinctive complementary absorption of spectral features through quantum state transitions. The relation between matter's color and color absorbed is shown in Table 1. The violet laser employed in the 3D sensor demonstrates spectral complementarity with green-yellow substrate. Based on the spectral analysis of the background substrate, this optical method effectively attenuates complementary transmitted laser through green-

yellow substrate, thereby suppressing scattering artifacts and specular reflection interference, as depicted in Figure 3.

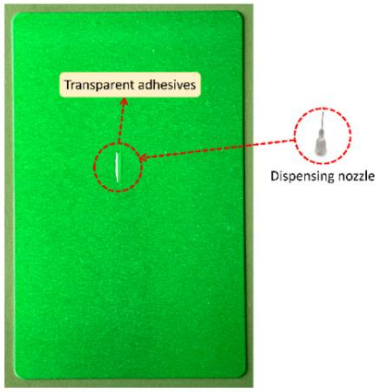

Figure 2. Schematic of designed transparent adhesives specimen.

Table 1. The relation between matter's color and color absorbed.

Light Absorbed		Perceived Complementary (Subtraction) Color
Wavelength(nm)	**Color**	
400-435	Violet	Green-yellow
435-480	Blue	Yellow
480-490	Green-blue	Orange
490-500	Blue-green(cyan)	Red
500-560	Green	Purple(magenta)
560-580	Yellow-green	Violet
580-595	Yellow	Blue
595-605	Orange	Green-blue
605-650	Redorange	Blue-green(cyan)
650-750	Red	Green

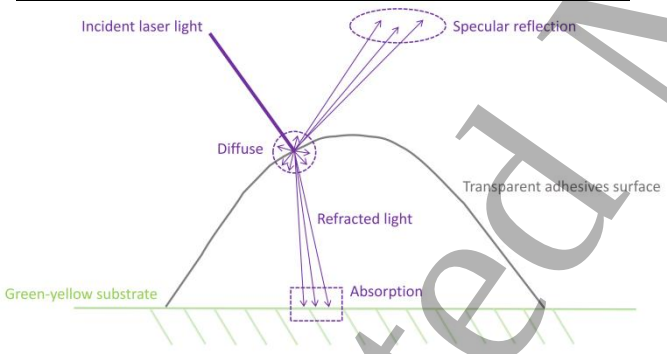

Figure 3. Schematic of complementary transmitted laser absorbed by green-yellow substrate.

2.2. 3D imaging system Calibration

The 3D line laser scanning system is shown in Figure 4. Designed specimen is mounted on a mobile robotic platform, where a laser emitter projects violet laser stripe onto the transparent adhesives dispensing region. Diffuse reflection occurs from the surface of the dispensed adhesives. The resultant reflected light is then guided through a lens assembly and imaged onto a high-precision CMOS sensor. In the system, camera calibration is essential for establishing a geometric mapping model between the image coordinate system and the world coordinate system. Achieving high-precision calibration and optimizing parameter accuracy constitute critical prerequisites for accurate 3D reconstruction. Conventional calibration methods typically involve a two-stage process. First, the intrinsic and extrinsic parameters of the camera are computed using at least 15 images captured from diverse poses. Second, the transformation between the camera coordinate system and the laser coordinate system is established. However, this approach is notably time-consuming and prone to cumulative errors due to its sequential nature. Errors from the first step may propagate to the second step, leading to uncontrollable error sources.

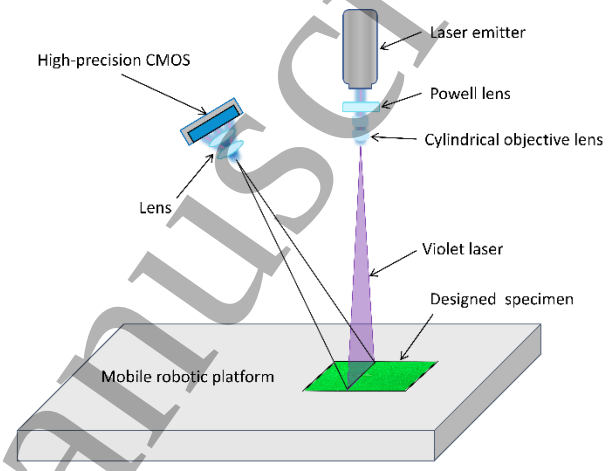

Figure 4. Schematic of 3D line laser scanning system.

We proposed an automatic camera calibration method to address the aforementioned issues. The proposed method first fixes the calibration board onto a precision lifting platform and installs a fixed illumination source within the camera's field of view for illuminating the calibration board. The platform is then moved to the initial plane at $\boldsymbol{Z} = 0$. The platform is raised by a predefined step size within the camera's field of view to reach a fixed position. The center points coordinate acquisition method is depicted in Figure 5. At each platform position, a laser stripe image is captured to extract the pixel coordinates $(\boldsymbol{u_i}, \boldsymbol{v_i})$ of the laser stripe center points. After turning on the light source and the laser source is turned off, an image of the calibration board is acquired. By merging the two images and interpolating using the known positions of the calibration points, the corresponding world coordinates $(\boldsymbol{x_i}, \boldsymbol{y_i}, \boldsymbol{z_i})$ of the center points are computed. The initial intrinsic and extrinsic parameters of the camera can be determined using the homography matrix, and the distortion coefficients are estimated using the nonlinear least squares method. Finally, all parameters are jointly optimized and refined based on the Maximum Likelihood Estimation (MLE) method to complete the camera calibration. The specific steps for parameter optimization are as follows:

- **Objective function formulation**

Assume the observation of 3D point coordinates $\boldsymbol{X}$ from the camera view is $\boldsymbol{x}$. Given the parameter set $\boldsymbol{\Theta}$ — including intrinsic parameters, extrinsic parameters for each view, and distortion parameters. The camera projection model (accounting for intrinsics, extrinsics, and distortion) is expressed as:

$$x = f(X; \Theta) + \varepsilon \#(3)$$

Where $\boldsymbol{f}: \boldsymbol{R^{3n}} \times \boldsymbol{R^{k}} \rightarrow \boldsymbol{R^{2mn}}$ is obtained by stacking n replicas of $\boldsymbol{f_1}, \ldots, \boldsymbol{f_m}$. $\boldsymbol{\varepsilon}$ is the residual vector. The problem of determining $\boldsymbol{\Theta}$ is most usefully cast as one of maximum likelihood estimation: the conditional probability: $\boldsymbol{\Lambda(\Theta)} = \boldsymbol{p(\varepsilon \mid \Theta, X)}$ called the likelihood function, and parameter estimation computes:

$$\hat{\Theta} = \underset{\Theta}{argmin} \Lambda(\Theta) \#(4)$$

Assuming independent Gaussian noise, the likelihood is the product of conditional probabilities over all observations. Taking the logarithm and discarding constant terms yields the negative log-likelihood, which is equivalent to the standard least-squares solution:

$$\hat{\Theta} = \underset{\Theta}{argmin} \epsilon^2(\Theta) \#(5)$$

Where $\boldsymbol{\epsilon(\Theta)} = \sqrt{\boldsymbol{\epsilon^T \epsilon}} = \| \boldsymbol{x} - \boldsymbol{f(X; \Theta)} \|$, and $\boldsymbol{\epsilon^2(\Theta)}$ is the scalar residual.

- **LM-based iterative optimization**

The parameter set $\boldsymbol{\Theta}$ is refined via the Levenberg–Marquardt algorithm:

$$\Theta^{(k+1)} = \Theta^{(k)} - [J^T W J + \lambda I]^{-1} J^T W \epsilon \#(6)$$

Where $\boldsymbol{J}$ is the Jacobian of residuals $\boldsymbol{\epsilon}$ with respect to $\boldsymbol{\Theta}$, $\boldsymbol{W}$ is the block-diagonal weight matrix from the residual covariance, and $\boldsymbol{\lambda}$ is the damping factor. Iterations continue until convergence in both parameter updates and objective value.

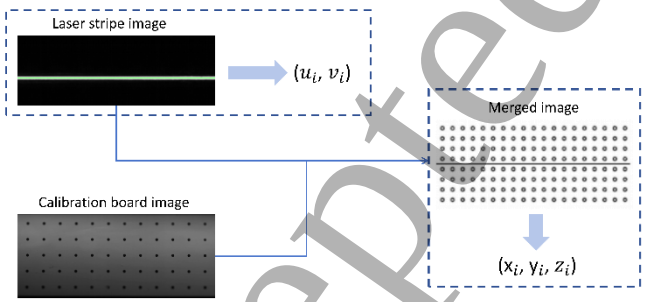

Figure 5. Schematic of center points coordinate acquisition method.

3. Method for 3D reconstruction

Through synchronized image data acquisition during planar scanning trajectories, cross-sectional contour profile image set of the adhesive specimen are obtained. The flowchart of 3D reconstruction is shown in Figure 6. The procedure after acquiring transparent adhesives contour profile images is divided into three steps: extraction of candidate points, post-processing of candidate points, depth map reconstruction. The role of each step is as follows:

1. The initial phase involves filtering out random noise through input image filter preprocessing. Subsequently, directional-consistency-verified gradient analysis is integrated with the gray-level center of gravity extraction algorithm to extract the set of sub-pixel multi-peak candidate center points. The details of this process are explained in 3.1.
2. The proposed DWMF-SS method conducts the preliminary screening of candidate points. This is followed by a secondary screening stage that incorporates position offset analysis and continuity length constraints. Finally, the linear interpolation algorithm is used for discontinuity region remediation to generate the laser stripe center line. This step is detailed in 3.2.
3. After obtaining the laser stripe center line, the corresponding world coordinates of individual contour points are computed based on system calibration parameters. In the final stage, all center lines are integrated into a depth map space to reconstruct the 3D surface of the transparent adhesives. This procedure is given in 3.3.

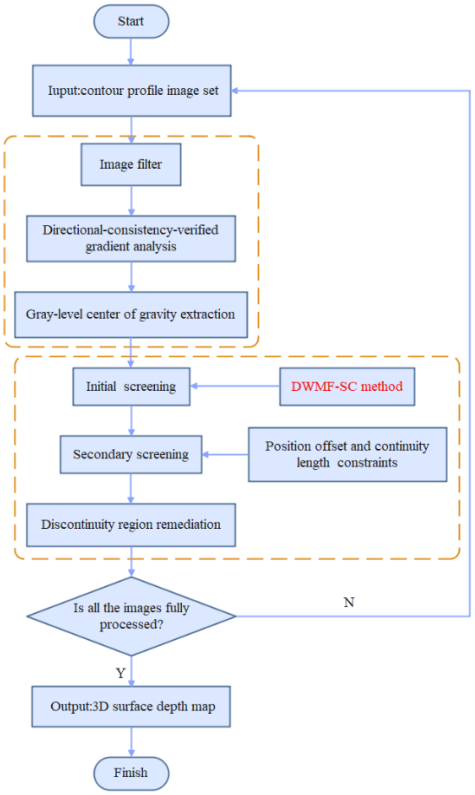

Figure 6. Flowchart of 3D reconstruction.

3.1. Extraction of candidate points

In order to mitigate interference from random noise, image smoothing is implemented in the image set through mean filtering. After that, each image in the image set is extracted separately for directional-consistency-verified gradient analysis to locate laser stripe candidate regions on a per-pixel-row basis. The schematic of candidate regions localization is shown in Figure 7. Based on the differences in gray-level value between neighboring pixels, this method is employed to validate candidate regions, with the specific principle described as follows:

$$\left.\begin{matrix} I_b - I_a \geq K \\ I_c - I_b \geq 0 \end{matrix}\right\} \rightarrow \mathrm{I}_{\text{Rising}} \in [a,c] \left.\begin{matrix} \\ \\ I_c - I_d \geq 0 \\ I_d - I_e \geq K \end{matrix}\right\} \rightarrow \mathrm{I}_{\text{Falling}} \in [c,e] \Bigg\} \rightarrow \mathrm{I} \in [b,d] \#(7)$$

Here, $\boldsymbol{I_a}$, $\boldsymbol{I_b}$, $\boldsymbol{I_c}$, $\boldsymbol{I_d}$, $\boldsymbol{I_e}$ is the gray-level value of the points $\boldsymbol{a}$, $\boldsymbol{b}$, $\boldsymbol{c}$, $\boldsymbol{d}$, $\boldsymbol{e}$. $\boldsymbol{K}$ denotes the edge detection gradient threshold, which can control the region edge. Consequently, the region $\mathrm{I}_{\text{Rising}}$ and $\mathrm{I}_{\text{Falling}}$ is categorized as gray-level rising delay and gray-level falling delay. Synthesizing the two parts delay leads to candidate region $\mathrm{I} \in [b,d]$ excluding the two endpoints. Analogously, candidate regions II and III are determined. Within each candidate region, candidate center points are calculated through gray-level center of gravity extraction method [23]. Assuming the column value range of candidate region is $\boldsymbol{x} \in [x_s, x_c]$ in a row, the conventional formula for gray-level center of gravity extraction algorithm is as follows:

$$x_{center} = \frac{\sum_{x=x_s}^{x_c} w\,(I_x) * x}{\sum_{x=x_s}^{x_c} w\,(I_x)} \#(8)$$

$$w(I_x) = \frac{I_x}{256 - I_x} \#(9)$$

Where, $\boldsymbol{I_x}$ is the gray-level value of point $\boldsymbol{x}$, $\boldsymbol{x_{center}}$ represents the column coordinate value of candidate center point. $\boldsymbol{w(I_x)}$ denotes gray-level density weighting model to highlight salient features within target area and improve localization accuracy. Finally, the positions of initial candidate points are extracted from each pixel row for the whole map.

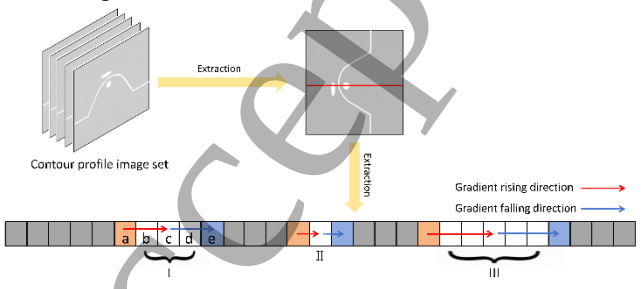

Figure 7. Schematic of candidate regions localization.

3.2. Post-processing of candidate points

Based on the extracted candidate points, we proposed the DWMF-SS method for preliminary screening of candidate points. The specific steps of this method are described below.

1)The first step is to analyze the continuity of the candidate points by searching for the neighboring preceding and subsequent rows of each candidate point and count the number of points that satisfy predefined position offset constraint. Position offset constraint is expressed using the following formula:

$$|x_c^{(k)} - \mathrm{x}_{neighbor}| \leq zValue \#(10)$$

Where, $\boldsymbol{x_c^{(k)}}$ represents column value at the ***k-th*** point form candidate point set $\boldsymbol{c}$ in a row, $\boldsymbol{x_{neighbor}}$ denotes the column value at the adjacent point form the preceding and subsequent row of ***k-th*** point, $\boldsymbol{zValue}$ indicates the maximum position offset threshold. Then, the normalized continuity score can be deduced:

$$S_{continuity}^{(k)} = \frac{L^{(k)}}{max(L)} \#(11)$$

Here, $\boldsymbol{L^{(k)}}$ is the number of points that satisfy predefined position offset constraint at ***k-th*** point. $\boldsymbol{max(L)}$ represents the maximum $\boldsymbol{L}$ among point set $\boldsymbol{c}$.

2)Furthermore, gray-level intensity score of ***k-th*** point can be determined as:

$$S_{intensity}^{(k)} = \frac{I^{(k)}}{I_{max}} \#(12)$$

Where, $\boldsymbol{I^{(k)}}$ is the gray-level value of ***k-th*** point, $\boldsymbol{I_{max}}$ is the maximum gray-level value among point set $\boldsymbol{c}$. In the third part, historical position score of ***k-th*** point is shown in the following formula:

$$S_{history}^{(k)} = 1 - \frac{|x_c^{(k)} - x_{prev}|}{R} \#(13)$$

Here, $\boldsymbol{x_{prev}}$ denotes column value at the initial screened point in the preceding row of ***k-th*** point, $\boldsymbol{R}$ is the normalization factor that can be expressed as the total number of columns or the maximum $\boldsymbol{x_{prev}}$ among point set $\boldsymbol{c}$.

3)After calculating the scores of the above three parts, the multi-factor dynamic weighted model was used to calculate the final score of k-th point:

$$\left.\begin{matrix} S_{final}^{(k)} = \alpha * S_{continuity}^{(k)} + \beta * S_{intensity}^{(k)} + \gamma * S_{history}^{(k)} \\ I^{(k)} < 0.1 * I_{max} \\ w > 20 \end{matrix}\right\} \rightarrow S_{final}^{(k)} = 0 \quad (14)$$

Where, $\boldsymbol{\alpha}$, $\boldsymbol{\beta}$, $\boldsymbol{\gamma}$ is the score weighting factors, $\boldsymbol{w}$ is the candidate region pixel width. For excluding invalid points, the points are filtered out both with gray-level value less than 10% of $\boldsymbol{I_{max}}$ among point set $\boldsymbol{c}$ and $\boldsymbol{w}$ larger than 20

pixel bits. The unique point in each row is obtained by calculating the maximum final score among point set $\boldsymbol{c}$.

As illustrated in Figure 8, there are $\boldsymbol{a}$ and $\boldsymbol{b}$ candidate points in the second row. These points are filtered by the DWMF-SS method to retain the optimal point. $\boldsymbol{zValue}$ is 5 pixel bit that represents the range of red arrows. Assuming the gray-level value $\boldsymbol{I^{(a)}} = 200$, $\boldsymbol{I^{(b)}} = 150$ at these points, $\boldsymbol{R} = 28$ can be described as the column value of image, the red point denotes the initial screened point in the first row. Obviously, the calculated result is $\boldsymbol{S^{(a)}_{final}} > \boldsymbol{S^{(b)}_{final}}$ so that the optimal point $\boldsymbol{a}$ is retained in the second row.

Figure 8. Illustration of DWMF-SS method.

Secondary screening applies the position offset and continuity length constraints to exclude anomalous jump region caused by random noise. This method initially detects the discrete start point of anomalous jump region, where the position offset from the preceding point exceeds a predefined threshold. When analysis reveals that the span of contiguous points from the start to end point remains below the predefined minimum continuity length, this identified region will be discarded.

In the ultimate stage, interpolated repair of contour interrupted regions is used to detect and locate the endpoints of fractured portion $\boldsymbol{P_1(x_1, y_1)}, \boldsymbol{P_2(x_2, y_2)}$. To avoid the generation of false interpolation points without real data support, the linear interpolation method [24] selectively reconstructs discontinuities only when the discontinuity length of interrupted region falls below the predefined interpolation threshold by constructing parametric linear equations $\boldsymbol{P(t) = P_1 + t(P_2 - P_1)}, \boldsymbol{t} \in [0,1]$. Based on sampling interval, absented point coordinates are calculated as follows:

$$\begin{cases} x_i = x_1 + \dfrac{i}{N}(x_2 - x_1) \\ y_i = y_1 + \dfrac{i}{N}(y_2 - y_1) \end{cases} \#(15)$$

$$i = 1, \ldots, N-1$$

$\boldsymbol{N}$ represents discontinuity length of interrupted region. Replenishing the set of points $\boldsymbol{(x_i, y_i)}$ reconstructs the complete center line of the laser stripe. A before-and-after comparison of the extracted true profile of the dispensed adhesives is presented in Figure 9.

Figure 9. Before-and-after comparison of the extracted true profile of the dispensed adhesives.

3.3. Depth map reconstruction

Upon extraction of the laser stripe center lines, the scanning system applies the system calibration parameters to calculate the world coordinates $\boldsymbol{(x, y, z)}$ of each contour point on the adhesive surface relative to the reference plane. The depth map [25] data space is a two-dimensional matrix containing depth ***Z-values*** and $\boldsymbol{X}$ and $\boldsymbol{Y}$ direction coordinate information. As shown in Figure 10, the spatial aggregation of all center lines is projected into a depth map space according to its spatial distribution characteristics. Therefore, spatial coordinates in $\boldsymbol{X}$, $\boldsymbol{Y}$ and $\boldsymbol{Z}$ axes are recorded in the true distance pixel units to generate the 3D surface depth map of the reconstructed transparent adhesives.

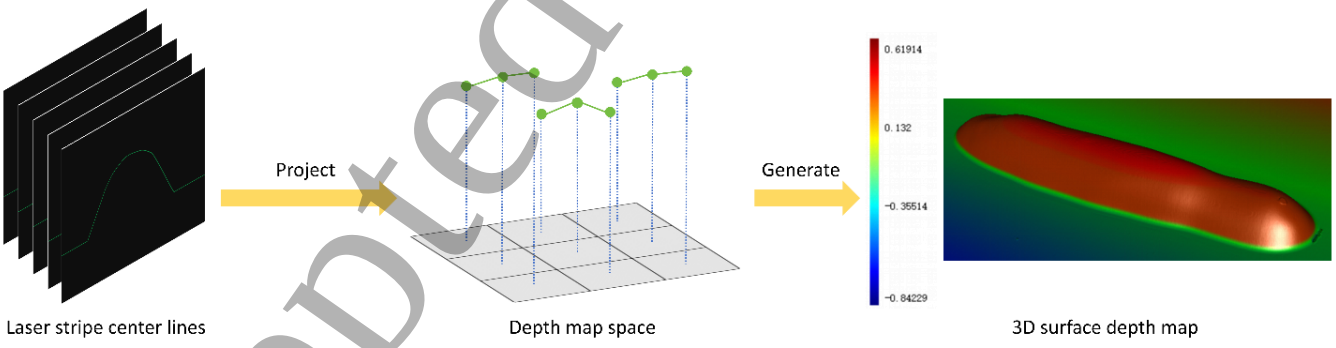

Figure 10. Schematic of transparent adhesives 3D surface depth map reconstruction.

4. Geometry analysis

With the obtained 3D surface depth map of the transparent adhesives, the geometric-based computational workflow for estimating transparent adhesives volume is shown in Figure 11.

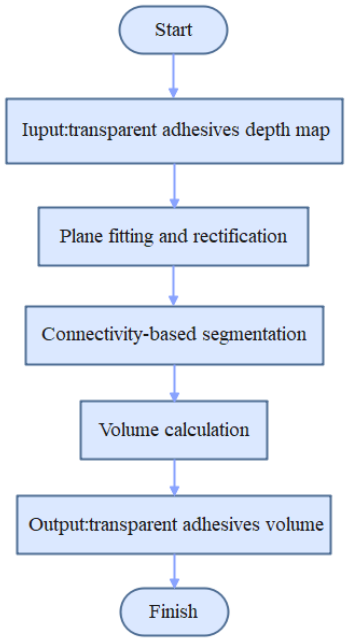

Figure 11. Flowchart of transparent adhesives geometry analysis.

4.1. Plane fitting and rectification

To process the reconstructed depth map, we employ several standard geometric analysis techniques, the measurement workflow initiates with defining a datum plane for the measured specimen to determine the optimal spatial distribution of depth map data for subsequent coordinate system unification.

Following datum plane calibration, the depth map data undergoes projective coordinate transformation to achieve geometric rectification with the reference coordinate system. This critical step ensures the accuracy, consistency, and comparability of final measurement results. As depicted in Figure 12, the general process of the method is as follows:

(1) With the yellow region of interest (ROI) designated as the target domain in the figure, obtaining randomly sa mpled regions of the platform depth map data serves a s the local plane fitting data.

(2) The plane fitting algorithm [26] based on well-established principal component analysis (PCA) is used to fit the ROI depth map data. The equation of the datum plane can be express as: $\boldsymbol{ax + by + cz + d = 0}$, where $\boldsymbol{a}$, $\boldsymbol{b}$, $\boldsymbol{c}$, and $\boldsymbol{d}$ are the fitted plane model parameters.

(3) After plane fitting computation, rigid-body transforma tion [27] is implemented to perform rotation and transl ation operations on the original depth map data. This method achieves data rectification by projecting data i nto the target plane coordinate system.

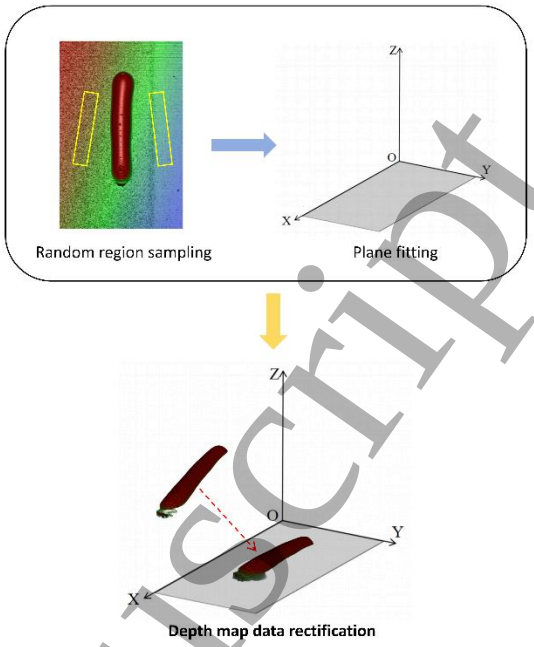

Figure 12. Schematic of plane fitting and rectification.

4.2 Connectivity-based segmentation

This step performs connectivity-based segmentation [28] on the depth map, as shown in Figure 13(a), to segment the background and isolate volume measurement regions specific to the transparent adhesives. This segmentation method first applies 3D Otsu thresholding algorithm [29] to generate a binarized image, and then traverses the image based on run-length encoding (RLE) [30]. Subsequently, it allocates regions across the entire image through eight-neighborhood connectivity analysis on encoded sequences, iterating until all connected regions are identified. Finally, geometric filtration is applied to extract the green connected domain representing convex depth features that exceed predefined depth threshold, as depicted in Figure 13(b).

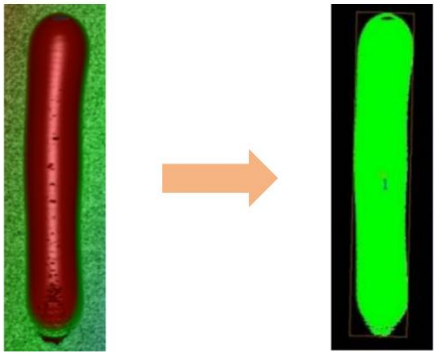

Figure 13. (a) Transparent adhesives depth map; (b) The result of connectivity-based segmentation method.

4.3 Volume calculation

Ultimately, as illustrated in Figure 14, the segmented adhesive volume measurement region undergoes geometric

decomposition where each pixel is regarded as an independent rectangular prism through the projection integration method [31]. The base dimensions of each prism correspond to the image's spatial resolution $\boldsymbol{\Delta x} \times \boldsymbol{\Delta y}$, while the height is defined by depth values $\boldsymbol{z_{xy}}$ from the calibrated depth map. The total adhesive volume is then calculated through volumetric integration of all individual prisms, expressed as:

$$V = (\Delta x * \Delta y) * \sum_{(x,y)\in R} z_{xy} \#(16)$$

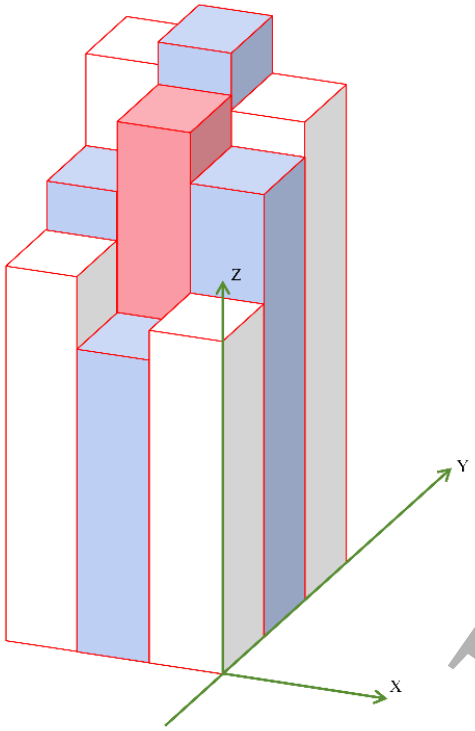

Figure 14. Schematic of projection integration volume algorithm.

5. Experiment and result analysis

5.1 Experimental setup

To validate the effectiveness and feasibility of the proposed method, we conducted various experiments on the experimental system. The system consists of two modules: an image acquisition and imaging module, and an image processing and control module. The image acquisition and imaging module is primarily composed of a laser emitter and a high-precision CMOS sensor with mobile robotic platform and test specimen. After image acquisition, the algorithm is implemented by a program written in C++ executed on the image processing and control module (a standard PC platform).

5.2 Experiments and comparisons of laser stripe centroid extraction

Comparative experiments were conducted between the proposed algorithm and other traditional algorithms, including the Steger [32], gray-level center of gravity, thinning algorithm [33]. To verify the robustness and stability of the proposed algorithm, we performed the experiment on an image with significant edge diffusion noise as shown in Figure 15. From the image, we can see that the profile of the laser stripe is uneven. Additionally, due to the metallic luster of the object's material, there are many edge diffusion noises in the image, which greatly affects the extraction of the center line of the laser stripe. This type of interference is commonly found in many metallic components. The extraction results (including the local magnification image) of the proposed algorithm and other traditional algorithms in this image are shown in Figure 16.

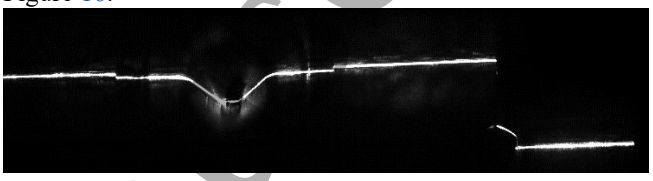

Figure 15. The original image of laser light stripe.

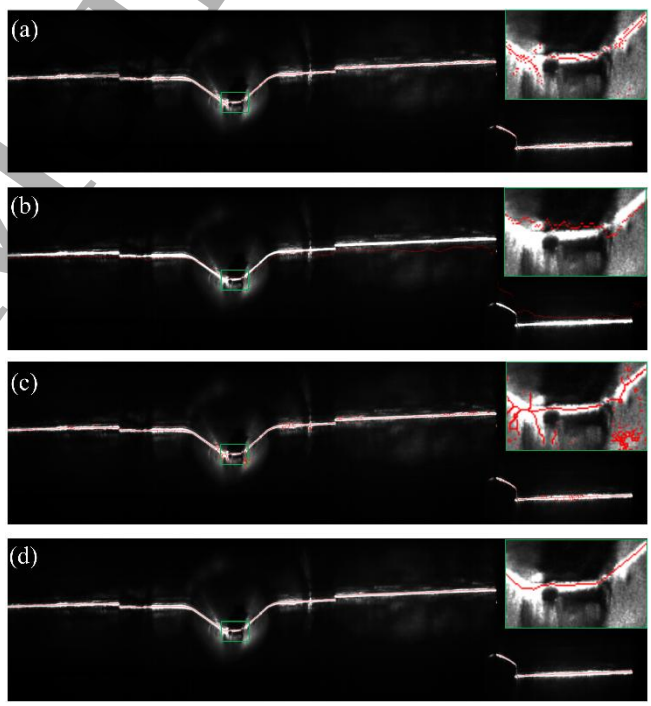

Figure 16. Extraction results comparison of algorithms. (a) The Steger method; The gray-level center of gravity method; (c) The thinning method; (d) The proposed method.

From the extraction result, the Steger method can preliminarily extract center points of the laser stripe. But since the laser stripe does not conform to a perfect Gaussian distribution and is affected by the edge diffusion noise, this results in complex light intensity distributions near the

edges. Such conditions can lead to erroneous extraction of multiple center points that erroneously incorporate noise points into the laser center line. The gray-level center of gravity method calculates the centroid for the entire column, which causes failure in accurate center line extraction of laser stripe under image noise interference. The thinning method is similarly compromised by edge diffusion noise, leading to erroneous skeleton extraction from noise points. In contrast, the proposed method demonstrates noise immunity and precisely extracts a set of center points that align well with the shape of the laser stripe. Additionally, the center points are extracted with great continuity and smoothness. This is because the algorithm uses the candidate points mechanism and takes advantage of the DWMF-SS method for candidate points selection, which effectively avoids the influence of noise.

The performance of the laser center line extraction algorithm is primarily evaluated based on accuracy and efficiency criteria. This paper adopts the approach from reference [34], using the root-mean-square deviation (RMSD) to characterize the accuracy of the algorithms in extracting the laser stripe center points. The RMSD represents the deviation between the extracted center points and the true center of center points. Since other traditional methods cannot correctly extract center points under strong interference, their calculated accuracy cannot be used as a reference. In this experiment, we utilize a calibration board specifically designed for 3D laser line scanning system calibration as the target object. As shown in Figure 17, the true center line of the horizontal laser stripe (indicated by the green line) is obtained. The experimental RMSD data for each algorithm are shown in Table 2. The RMSD is:

$$RMSD = \sqrt{\frac{\sum_{i=1}^{n}(y_i - y)^2}{n}} \#(17)$$

where $\boldsymbol{n}$ is the number of center points, $\boldsymbol{y_i}$ is the calculated row value of the center point and $\boldsymbol{y}$ corresponds to the true row value of each center point.

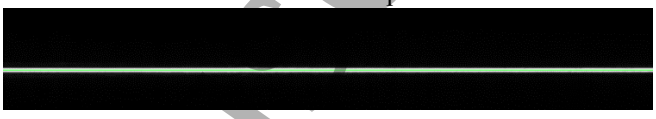

Figure 17. The laser light stripe of calibration board with gre en true center line.

Table 2. RMSD comparison of each algorithm.

Algorithm	Steger	Gray-Scale Center of Gravity	Thinning	Our Method
RMSD (pixels)	0.2657	1.0253	0.1518	0.0682

From the experimental results presented in the table, the proposed algorithm achieves 74%, 93%, and 55% error reduction compared to the Steger method, gray-level center of gravity method, and thinning method, respectively. This experiment demonstrates that the proposed algorithm has high precision while better satisfying industrial measurement accuracy requirements. To evaluate the extraction efficiency of the proposed algorithm, we compared the computational time required by each algorithm to process original laser stripe image under strong interference conditions, as mentioned earlier. The average extraction time across multiple repeated measurements was calculated. The average extraction times of the algorithms are presented in Table 3.

Table 3. The average extraction time of each algorithm.

Algorithm	Steger	Gray-Scale Center of Gravity	Thinning	Our Method
Runtime (s)	0.0247	0.0047	0.0168	0.0053

From the table, the experimental data proved that the speed of the proposed algorithm is 4.66 times faster than the Steger algorithm, 3.17 times faster than the thinning algorithm, whereas it exhibits 1.13 times slower compared to the gray-level center of gravity algorithm. This performance difference originates from the algorithm's need to process additional candidate points along the laser stripe periphery, which marginally compromises computational efficiency. Nevertheless, the proposed algorithm still maintains sufficient processing speed to satisfy industrial real-time requirements.

To determine the optimal score weighting factors for candidate points in the DWMF-SS algorithm, we conducted comparative laser stripe centroid extraction experiment of six different sets of weighting factors using the image shown in Figure 15. A comparison of the magnified extraction results from six different sets of weighting factors is presented in Figure 18.

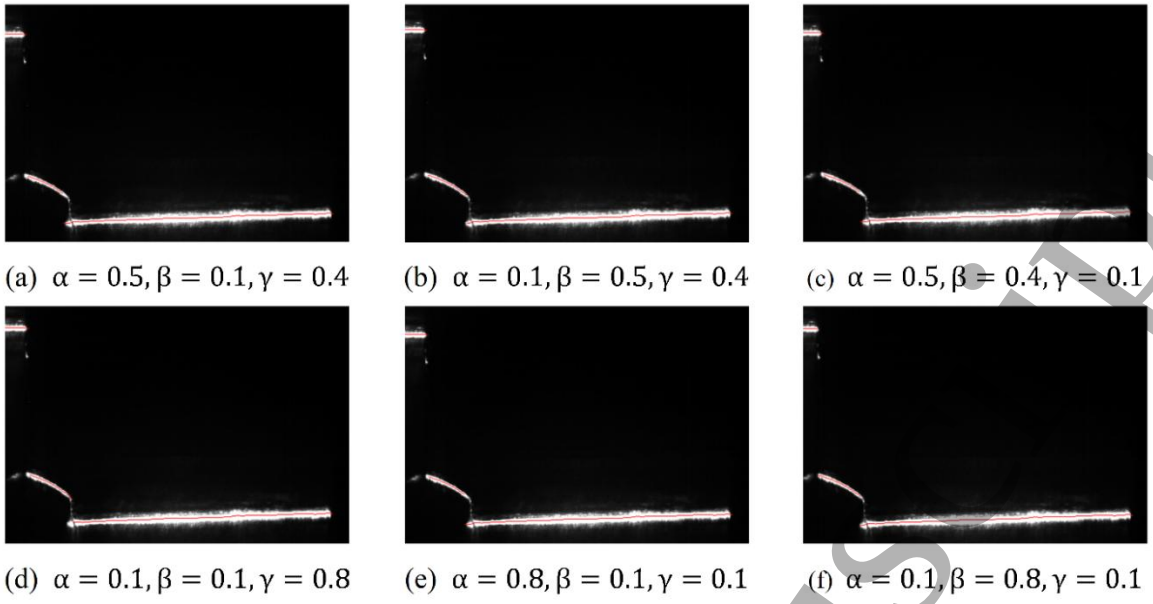

Figure 18. A comparison of the magnified extraction results from six different sets of weighting factors.

The results indicate that, under image noise interference, the set (f) of weighting factors outperformed the others, producing extracted lines that closely matched the actual contour. Therefore, $\boldsymbol{\alpha} = 0.1$, $\boldsymbol{\beta} = 0.8$, $\boldsymbol{\gamma} = 0.1$ was selected as the final score weighting factors for candidate points calculation in the DWMF-SS algorithm. To evaluate the applicability and noise robustness of the proposed algorithm, images were acquired in a complex factory environment under varying noise levels, camera exposures, and reflection interferences. These images were processed using our method, and the corresponding results are shown in Figure 19.

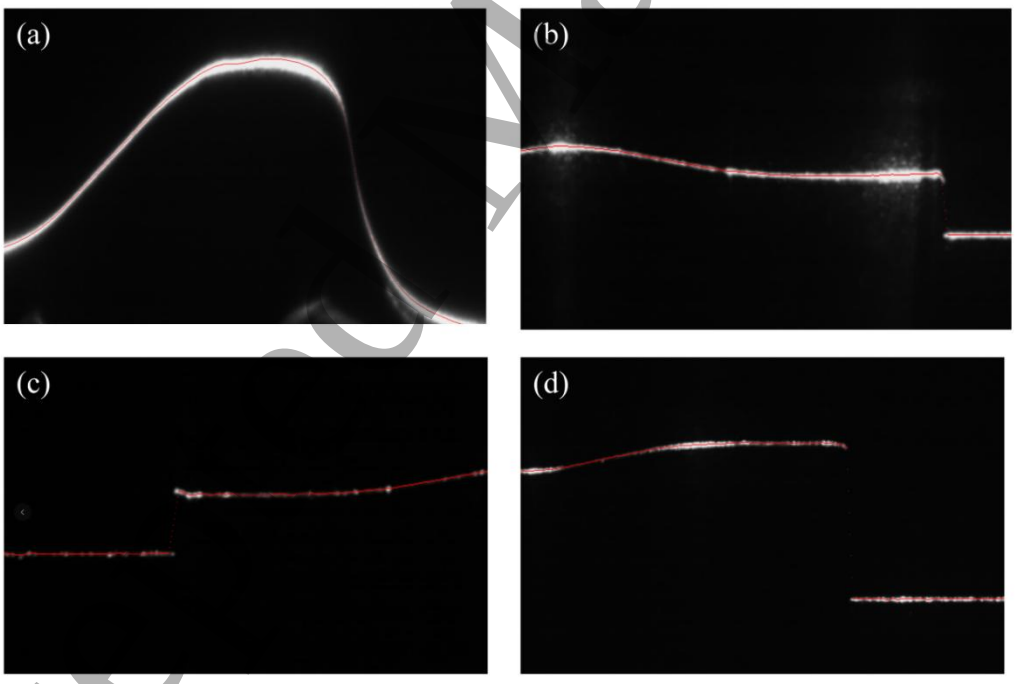

Figure 19. The Extraction results of the images using our method.

It can be observed from the Figure that the our algorithm delivers effective results, demonstrates wide applicability, and exhibits great noise robustness.

5.3 Experiment of volume measurement

To validate the effectiveness of the proposed CSBO method, we conducted comparative analyses using transparent adhesives specimens. First, the experimental setup employed a precision dispensing nozzle to extrude similar linear transparent adhesives beads onto five

distinctive color (green-yellow, blue, pink, purple, black) background substrate, detailed in Figure 20. Then the dispensed adhesives specimens were weighed using a precision electronic balance as shown in Figure 21, with the measured mass systematically documented as reference true value. Experimental verification was performed using the previously described 3D line laser scanning system in a workshop environment to collect the surface data of the specimens. After that, the image processing module implemented 3D surface reconstruction and volume measurement of dispensed adhesives through a series of proposed algorithms.

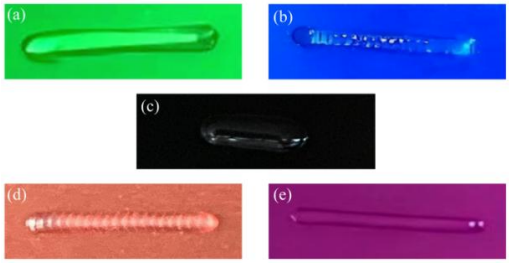

Figure 20. The designed five different specimens.

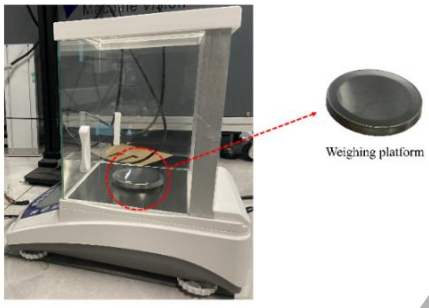

Figure 21. The experimental precision electronic balance.

To minimize random variability, we performed five experimental replicates for each of the four distinct color substrates. Within each replicate, the volume of the dispensed transparent adhesives was measured 20 times, and the standard deviation $\boldsymbol{\sigma}$ of these measurements was subsequently calculated to assess the variability across repeated trials. The arithmetic mean of these 20 measurements was then calculated and recorded as the final result for that replicate. Assuming the transparent adhesives density value is $\boldsymbol{\rho}$ and predicted volume value is $\boldsymbol{V}$, the relative error ratio of volume measurement can be expressed mathematically as:

$$\delta = \frac{\Delta}{G_t} * 100\% \#(18)$$

Here, $\boldsymbol{\Delta = |G_t - G|}$ denotes absolute error of volume measurement, $\boldsymbol{G_t}$ represents the ground truth (GT) weight of dispensed adhesives, $\boldsymbol{G = V * \rho}$ is the measure weight of dispensed adhesives. The experimental results of each specimen volume measurement are shown in Table 4. For better visualization, the average relative error ratio of each specimen was transformed into the histogram shown in Figure 22.

Table 4. Volume measurement experimental result between the proposed method and other methods.

Test specimen	NUM	GT weight (g)	Volume (mm3)	Standard deviation(σ)	Measure weight (g)	Relative error (%)
Specimen 1 Green-yellow color ρ=0.0011(g/mm3)	1	0.0145	12.997982	0.01260	0.014298	1.39%
	2	0.0201	17.862304	0.00406	0.019649	2.25%
	3	0.0212	19.696429	0.01812	0.021666	2.20%
	4	0.0331	29.747193	0.00840	0.032722	1.14%
	5	0.0274	24.633830	0.01774	0.027097	1.11%
Specimen 2 Blue color ρ=0.0011(g/mm3)	1	0.0124	10.252148	0.01752	0.011277	9.05%
	2	0.0378	31.488689	0.04463	0.034638	8.37%
	3	0.0324	31.867999	0.04934	0.035055	8.19%
	4	0.0316	25.976667	0.06645	0.028574	9.58%
	5	0.0308	25.586820	0.06609	0.028146	8.62%

Specimen 3 Pink color ρ=0.0011(g/mm3)	1	0.0152	12.708621	0.00206	0.013979	8.03%
	2	0.0283	23.729974	0.01910	0.026103	7.76%
	3	0.0315	26.017456	0.09560	0.028619	9.15%
	4	0.0316	26.504059	0.06890	0.029154	7.74%
	5	0.0263	21.642158	0.02561	0.023806	9.48%
Specimen 4 Purple color ρ=0.0011(g/mm3)	1	0.0108	8.971243	0.00411	0.009868	8.63%
	2	0.0413	34.652373	0.03434	0.038118	7.71%
	3	0.0365	30.491767	0.04893	0.033541	8.11%
	4	0.0318	31.271675	0.06724	0.034399	8.17%
	5	0.0277	27.399781	0.05287	0.030140	8.81%
Specimen 5 Black color ρ=0.0011(g/mm3)	1	0.0168	14.630526	0.02648	0.016094	4.20%
	2	0.0183	17.417592	0.01113	0.019159	4.70%
	3	0.0271	23.495281	0.00479	0.025845	4.63%
	4	0.0345	29.986199	0.01295	0.032985	4.39%
	5	0.0359	31.290007	0.01036	0.034419	4.13%

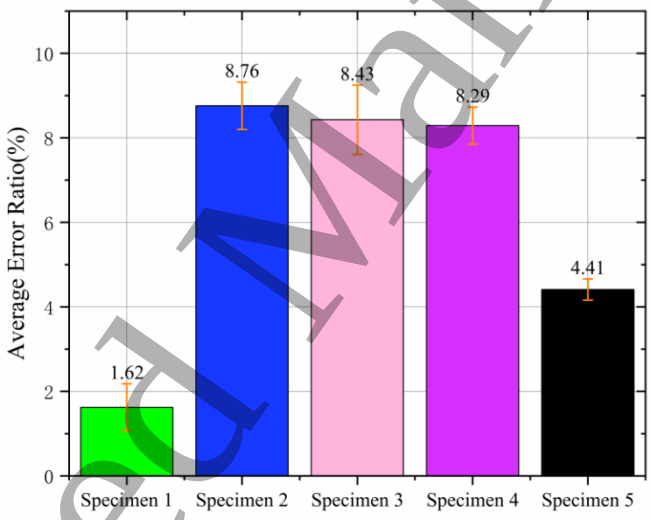

Figure 22. Comparison of the average relative error ratio of each specimen (Error bars indicate the standard deviation of the average error ratio).

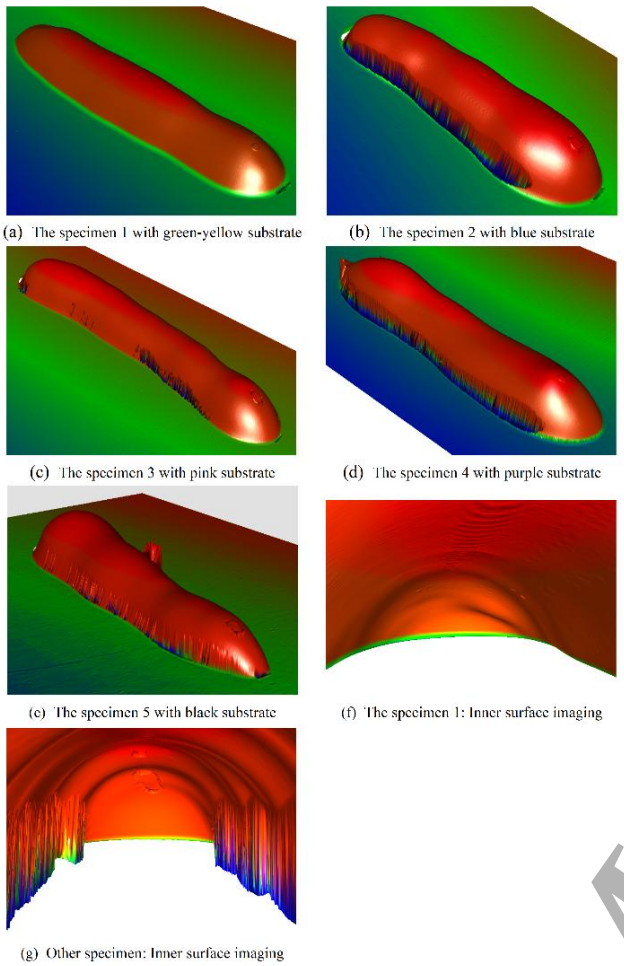

Figure 23. 3D reconstruction results of each specimen.

From the table and histogram experimental data, we can see that the average error ratio of specimen 1 with green-yellow substrate is about 4 times lower than the others, which can reach about 1.62%. The 3D reconstruction results of each specimen are shown in Figure 23. A comparison of 3D reconstruction results reveals that the depth map of dispensed transparent adhesives obtained via the proposed CSBO method exhibits greater completeness and surface smoothness than those from competing methods, leading to superior 3D shape measurement accuracy. In contrast, depth maps acquired through other methods exhibit varying degrees of surface reconstruction distortion due to internal optical interference. Based on the spectral analysis of the background substrate, a complementary green-yellow substrate was selected. Experimental validation confirmed that the green-yellow substrate exhibited the best performance under violet laser illumination.

To verify the effectiveness of the system in measuring nonlinear or more complex adhesive shapes, we employed a precision dispensing nozzle to extrude six groups of transparent adhesives beads with different shapes onto green–yellow background substrate. Using our system to individually test each of these six specimens, we then utilized the resulting data to perform the statistical analysis and data evaluation methods discussed in our study. The experimental results of six groups transparent adhesives volume measurement are shown in Table 5. The 3D reconstruction results of six groups specimen are shown in Figure 24.

Table 5. Volume measurement experimental result of the six groups specimen.

Test specimen	NUM	GT weight (g)	Volume (mm3)	Standard deviation(σ)	Measure weight (g)	Relative error (%)
Curvilinear bead patterns ρ=0.0011(g/mm3)	a	0.0192	17.038216	0.03301	0.018742	2.38%
	b	0.0189	16.224680	0.01081	0.017847	5.57%
	c	0.0196	16.287939	0.03229	0.017917	8.59%
Annular bead patterns ρ=0.0011(g/mm3)	d	0.0214	19.876290	0.02497	0.021864	2.17%
	e	0.0145	13.915174	0.03851	0.015307	5.56%
	f	0.0343	29.569542	0.02632	0.032526	5.17%

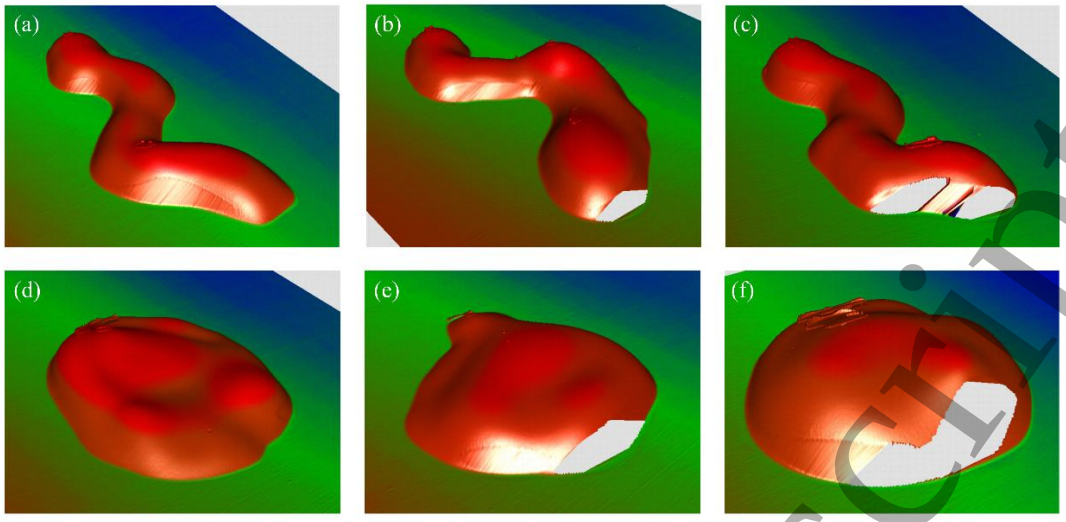

Figure 24. 3D reconstruction results of the six groups specimen.

From the experimental table and figure, the tested specimens were categorized into two groups: specimens (a), (b), and (c) were classified as curvilinear bead patterns, whereas specimens (d), (e), and (f) corresponded to annular bead patterns. It is observed that the relative error ratio of specimen (a) and (d) remains at approximately 2%, thereby demonstrating consistently high accuracy. However, the relative error ratio of specimen (b), (c), (e), and (f) exhibited a more pronounced increase and fluctuation, which can be primarily attributed to the fact that, as revealed in the 3D reconstruction results, the corresponding depth maps of these groups exhibited varying degrees of reconstructed surface data loss. According to the principle of laser triangulation, when the front surface of the workpiece exhibits a complex geometry or increased thickness, the camera's line of sight is occluded, resulting in field-of-view blind spots in the rear regions and consequently causing missing scan surface data. This phenomenon represents an inherent limitation of line laser scanning systems. Currently, the mainstream approach to address this issue is to perform two separate scans from different viewpoints, allowing the previously occluded regions to be captured during the second scan. By merging the data from both scans, the missing scan information in the rear regions can be effectively recovered.

6 Conclusions

To overcome the inaccuracy, inefficiency, and high equipment costs of traditional measurement methods for calibration of transparent adhesives discharge, we designed a line laser scanning volume measurement system. An automatic camera calibration method was proposed to simplify the calibration process and eliminate secondary calibration steps. By utilizing a unique candidate points mechanism and the novel DWMF-SS method for candidate points screening, we develop an improved gray-level center of gravity extraction algorithm, which can enhance process stability and selection accuracy. Based on the spectral analysis of the background substrate, we proposed the CSBO method to suppress internal scattering and reflection interference without complex ray-tracing algorithms and auxiliary equipment.

Experimental results show that the proposed centroid extraction method achieves smooth and continuous stripe profiles, processes images with edge diffusion noise at industrial real-time speeds, and attains the RMSD of 0.0682 pixels—significantly lower than other methods. In our system, FPGA-based hardware acceleration enables pixel-stream real-time processing, where noise filtering, gradient analysis, candidate scoring, interpolation, and centroid extraction are executed in parallel within a single clock cycle. On our test hardware, the maximum processing speed reaches 18 kHz (≈55.6 μs per frame), which fully meets industrial real-time requirements. Using the improved laser stripe centroid extraction algorithm, the CSBO-based volume measurement achieved the lowest relative error ratio of only 1.62%. These experimental measurement results fully prove that the green-yellow substrate exhibited the best performance under violet laser illumination. Future developments will aim to refine the proposed system for calibration of transparent adhesives discharge under complex backgrounds, and further investigate techniques for supplementing or optimizing single-scan data to address the issue of missing information in individual scans.

Data availability statement

All data that support the findings of this study are included within the article (and any supplementary files).

Acknowledgments

This research is fully conducted and supported by OPT Machine Vision. The authors would like to thank Prof. Daquan Feng for his valuable tutorial guidance and constructive review advice of the manuscript.

References

[1] Huang B, Liu X, Yan J, Xie J, Liu K, Xu Y, Liu J and Zhao X 2023 Fully automated dispensing system based on machine vision Applied Sciences 13 9206

[2] Ulkundakar N, Savarapu R and Kollu P 2022 Design, simulation and fabrication of non-spiral based fluxgate sensor on printed circuit board (PCB) Journal of Magnetism and Magnetic Materials 562 169769

[3] Hottinger C and Meindl J 2005 Unambiguous measurement of volume flow using ultrasound Proceedings of the IEEE 63 984–5

[4] Sharma J N, Pattadar D K, Mainali B P and Zamborini F P 2018 Size determination of metal nanoparticles based on electrochemically measured surface-area-to-volume ratios Analytical chemistry 90 9308–14

[5] Liu Y, Guo Y, Fan Y, Zhou J, Li Z, Xiao S, Zhang X and Wu G 2024 Optical imaging technology application in transmission line insulator monitoring: A review IEEE Transactions on Dielectrics and Electrical Insulation 31 3120–32

[6] Hu F, Zhu W, Huang W and Xu J 2023 Precise Phase Measurement for Fringe Reflection Technique through Optimized Camera Response Sensors 23 9299

[7] Ishii I, Yamamoto K, Doi K and Tsuji T 2007 High-speed 3D image acquisition using coded structured light projection 2007 IEEE/RSJ International Conference on Intelligent Robots and Systems (IEEE) pp 925–30

[8] Zhao X, Yu T, Liang D and He Z 2024 A review on 3D measurement of highly reflective objects using structured light projection The International Journal of Advanced Manufacturing Technology 132 4205–22

[9] Lu L, Bu C, Su Z, Guan B, Yu Q, Pan W and Zhang Q 2024 Generative deep-learning-embedded asynchronous structured light for three-dimensional imaging Advanced Photonics 6 046004–046004

[10] Hernandez C, Vogiatzis G and Cipolla R 2008 Multiview photometric stereo IEEE Transactions on Pattern Analysis and Machine Intelligence 30 548–54

[11] Huang S, Shi Y, Li M, Qian J and Xu K 2023 Underwater 3D reconstruction using a photometric stereo with illuminance estimation Applied Optics 62 612–9

[12] Jin S, Cho J, Dai Pham X, Lee K M, Park S-K, Kim M and Jeon J W 2009 FPGA design and implementation of a real-time stereo vision system IEEE transactions on circuits and systems for video technology 20 15–26

[13] Zheng H, Duan F, Li T, Li J, Niu G, Cheng Z and Li X 2023 A stable, efficient, and high-precision non-coplanar calibration method: applied for multi-camera-based stereo vision measurements Sensors 23 8466

[14] Zhang Q, Liu F, Lu L, Su Z, Pan W and Dai X 2024 Reconstruction of transparent objects using phase shifting profilometry based on diffusion models Optics Express 32 13342–56

[15] Green B L, Collins A T and Breeding C M 2022 Diamond spectroscopy, defect centers, color, and treatments Reviews in Mineralogy and Geochemistry 88 637–88

[16] Trivedi V, Joglekar M, Mahajan S, Patel N, Chhaniwal V, Javidi B and Anand A 2019 Digital holographic imaging of refractive index distributions for defect detection Optics & Laser Technology 111 439–46

[17] He K, Sui C, Huang T, Zhang Y, Zhou W, Chen X and Liu Y-H 2022 3D surface reconstruction of transparent objects using laser scanning with a four-layers refinement process Optics Express 30 8571–91

[18] He K, Sui C, Huang T, Dai R, Lyu C and Liu Y-H 2022 3D Surface reconstruction of transparent objects using laser scanning with LTFtF method Optics and Lasers in Engineering 148 106774

[19] Pan W, Jiang B, Tang W, Wu F and Li S 2024 Gap measurement method based on projection lines and convex analysis of 3D points cloud Measurement Science and Technology 35 105024

[20] Jiang H, Fu W, Zhang X and Zhang C 2024 Extraction of laser stripe centerlines from translucent optical components using a multi-scale attention deep neural network *Measurement Science and Technology* **35** 085404

[21] Kume A 2017 Importance of the green color, absorption gradient, and spectral absorption of chloroplasts for the radiative energy balance of leaves Journal of plant research 130 501–14

[22] Beard M C, Blackburn J L, Johnson J C and Rumbles G 2016 Status and Prognosis of Future-Generation Photoconversion to Photovoltaics and Solar Fuels ACS Energy Letters 1 344–7

[23] Huang Y, Kang W and Lu Z 2024 Improved Structured Light Centerline Extraction Algorithm Based on Unilateral Tracing Photonics vol 11 (MDPI) p 723

[24] Chen X, Xie Z, Eun Y, Bettens A and Wu X 2023 An observation model from linear interpolation for quaternion-based attitude estimation IEEE Transactions on Instrumentation and Measurement 72 1–12

[25] Fan Y-C, Huang C J and Yelamandala C M 2023 Image Recognition Based on High Accuracy 3D Depth Map Information Journal of Advances in Information Technology 14 1082–7

[26] Zhou J, Jin W, Wang M, Liu X, Li Z and Liu Z 2023 Improvement of normal estimation for point clouds via simplifying surface fitting Computer-Aided Design 161 103533

[27] Marker P, Jirasek R, Schmidt T and Bleicher A 2023 Development, realization, and experimental validation of an active hybrid roof structure based on elastic kinetic and rigid-body transformation International Journal of Space Structures 38 83–100

[28] Yang Z and Farsiu S 2023 Directional connectivity-based segmentation of medical images Proceedings of the IEEE/CVF conference on computer vision and pattern recognition pp 11525–35

[29] He Y, Hu Z, Wang R, Zhu H and Fu G 2024 Features extraction of point clouds based on Otsu's algorithm Measurement Science and Technology 35 065205

[30] Rongali A S, Dhabliya D, Pandey I, Sachdeva A, Praveena H D and Aich S C 2024 Investigating Applications of Run Length Encoding in Data Compression & Source Coding 2024 15th International Conference on Computing Communication and Networking Technologies (ICCCNT) (IEEE) pp 1–5

[31] Wang J and Ren X 2023 A consistent projection integration for Galerkin meshfree methods Computer Methods in Applied Mechanics and Engineering 414 116143

[32] Lai M, Liu X, Wang S, Jiang H, Li G and Cui J 2023 Realizing quality inspection in magnetic pulse crimping manufacturing:

Using Steger algorithm and self-attention Journal of Materials Processing Technology 311 117799

[33] Niu W, Chen Z, Zhu Y, Sun X and Li X 2022 Track line recognition based on morphological thinning algorithm Applied Sciences 12 11320

[34] Zhang M, Li Z, Zhang F and Ma L 2022 Adaptive bidirectional gray-scale center of gravity extraction algorithm of laser stripes Sensors 22 9567